# First Performance Measurements of the Phase Four RF Thruster

**IEPC-2017-431**

*Presented at the 35th International Electric Propulsion Conference*
*Georgia Institute of Technology – Atlanta, Georgia – USA*
*October 8–12, 2017*

M. Umair Siddiqui,* Chris Cretel,† and Joshua Synowiec‡
*Phase Four, Inc., El Segundo, CA, 90245, USA*

Andrea G. Hsu,§ Jason A. Young,¶ and Rostislav Spektor‖
*The Aerospace Corporation, El Segundo, CA, 90245, USA*

**Abstract: We present the first performance measurements of the Phase Four RF Thruster (RFT) from testing performed at The Aerospace Corporation and at Phase Four laboratories. The RFT is a nano-satellite-scalable, electrothermal RF thruster in development that uses RF power to heat xenon plasma propellant, and accelerate it in a radially diverging magnetic plume. For the measurements at The Aerospace Corporation, the proof-of-concept RFT-0 unit was integrated into a 3D printed test bus, which contained a laboratory xenon propellant management unit (PMU), and an on-board control computer, in a 3U CubeSat form factor. Subsequent probe measurements on the RFT-0 and the updated RFT-2 thrusters were performed at the Phase Four laboratory. Presented measurements include RFT-0 direct thrust on a torsional balance thrust stand, and Faraday and Langmuir probe measurements in the plume for both the RFT-0 and the RFT-2. Measurements show that the RFT-0 performance meets that of existing, higher power and heavier RF thrusters that have been measured on thrust stands. Probe measurements suggest that RFT-2 is making significant progress towards extending the measured RFT-0 performance to higher values of specific impulse.**

*Chief Technology Officer, Phase Four, Inc., umair@phasefour.io
†Propulsion Test Engineer, Phase Four, Inc., chris@phasefour.io
‡Aerospace Systems Engineer, Phase Four, Inc., josh@phasefour.io
§Member of the Technical Staff, Propulsion Science Department, andrea.g.hsu@aero.org
¶Member of the Technical Staff, Propulsion Science Department, jason.a.young@aero.org
‖Section Manager, Propulsion Science Department. rostislav.spektor@aero.org

## Nomenclature

$A$ = area of calibration electrodes, $m^2$
$b$ = damping constant of the thrust stand, kg/s
$D$ = distance between calibration electrodes, m
$e$ = fundamental charge, C
$F$ = force between calibration electrodes, N
$F_{cg}$ = cold gas thrust, N
$F_T$ = thrust force, N
$\delta F_T$ = thrust uncertainty, N
$g_0$ = Earth surface acceleration rate, $m/s^2$
$I_{sp}$ = specific impulse, s
$I_{sat}$ = ion saturation current on Langmuir/Faraday probe, A
$k$ = torsional spring constant, N-m/rad
$L$ = length of thrust stand moment arm, m
$M$ = effective mass of thrust stand and test bus at the moment arm location, kg
$M_{xe}^{amu}$ = xenon mass, amu
$\dot{m}$ = propellant mass flow rate, kg/s
$\delta\dot{m}$ = propellant mass flow rate uncertainty, kg/s
$\dot{m}_{ing}$ = ingested mass flow into thruster, kg/s
$P$ = power to the thruster, W
$P_{ch}$ = pressure in the vacuum chamber, Torr
$T_e$ = electron temperature, eV
$T_g$ = background chamber gas temperature, K
$\Delta t$ = hot fire thrust duration, s
$V$ = voltage bias between calibration electrodes, V
$x(t)$ = displacement of the thrust stand vs. time, m
$x_0$ = amplitude of step function displacement of the thrust stand, m
$\alpha$ = area of thruster orifice, $m^2$
$\epsilon_0$ = permitivitty of free space, Farads/m
$\gamma$ = damping rate of the thrust stand oscillations, $s^{-1}$
$\eta_T$ = thrust efficiency
$\eta_c$ = Clausing's factor
$\eta_{div}$ = divergence efficiency
$\theta$ = angular displacement of thrust stand, rad
$\theta_p$ = angular position of Faraday probe, rad
$\phi$ = phase of thrust stand response to applied step force, radians
$\omega$ = resonant frequency of the thrust stand, rad/s

# I. Introduction

RADIO frequency thrusters are electric propulsion systems that use radio frequency electromagnetic signals to accelerate a plasma propellant, generating thrust. RF thrusters vary widely in power budget and plasma-acceleration mechanism. Electromagnetic RF thrusters, such as the multi-kW scale VAriable Specific Impulse Magnetoplasma Rocket (VASIMR) engine[1] and the lower power Beating Electrostatic Wave (BEW) thruster concept,[2] use electromagnetic forces to accelerate ions. Electrostatic RF thrusters, such as the Helicon Double Layer Thruster (HDLT)[3] and the Neptune thruster,[4] use both free standing DC and applied RF electric fields to accelerate ions. Electrothermal RF thrusters, such as the Phase Four RFT and electron cyclotron resonance thrusters[5,6] drive ion acceleration primarily through heating of constituent plasma particles via the applied RF signals. Using RF systems for electric propulsion presents several advantages. First, a considerable knowledge base of RF plasma generation and heating has already been established through on-going efforts in the plasma processing and plasma fusion communities.[7,8] Second, RF plasma systems can efficiently generate very highly ionized plasmas with relatively moderate to low input RF power, ultimately increasing an RF thruster's efficiency.[9–11] Third, RF electronic active components have been miniaturized largely through the progress made by the cellular and wireless power industries,[12] increasing their suitability for low mass budget spacecraft applications.

This paper concerns the development of the Phase Four Radio Frequency Thruster (RFT). The RFT is a miniaturized electrothermal RF thruster that is designed to scale down to the mass, volume and power budget of Cube Satellites (CubeSats), to meet the propulsion needs of the upcoming constellations of "small" ($\approx 5$ to $\approx 500$ kg) satellites, as well as some propulsion needs for all-electric satellite buses. We describe the first performance measurements of the RFT proof-of-concept (RFT-0), as well as progress made on the design with the next generation thruster (RFT-2). In Section II we provide a high level description of the RFT, as well as introduce the nomenclature for RFT developmental generations. In Section III we describe the experimental setup and test results from direct thrust testing of the initial RFT-0. In Section IV we describe the experimental setup and test results of probe measurements in the plumes of both the initial RFT-0 and the RFT-2. Finally, in Section V we provide a summary and outlook for RFT development. We do not provide specific details on internal geometries of thruster components, such as the magnets, fields, liner, antenna or specific operational frequencies, due to their proprietary nature to Phase Four, Inc. In some figures, some internal geometries are purposefully misrepresented for the same reason. Furthermore, we do not go into detail on the specific physics of particle heating and acceleration in miniaturized RF thruster systems. As such, the data here will not be presented in a manner so as to defend the claims made on the operational mechanics of the thruster. These topics may be discussed in subsequent disclosures should Phase Four deem appropriate. Furthermore, this paper will not be describing the proprietary solutions to a series of problems Phase Four has solved over the past 18 months including: small RF plasma ignition, propellant storage and delivery for CubeSats, efficient RF signal generation from low power buses, propellant fill operations for small satellites, electric propulsion system on orbit operations for small satellites, and compensation for magnetic dipole-induced spacecraft torques.

# II. The Phase Four Radio Frequency Thruster

Figure 1 shows a representative diagram of the core components of the Phase Four RFT. A qualitative description of the RFT is as follows: xenon gas is injected into a ceramic "plasma liner" (shown in purple in Fig. 1). The liner is wrapped in an inductive RF coil (called the "antenna") through which an alternating current is driven at a specified RF frequency in the high frequency (HF) band. The liner and antenna are themselves positioned inside a permanent magnet-generated magnetic field. The fields have a specified strength as a function of position within the plasma liner, which rapidly expands radially in the reference frame of an accelerated plasma particle traveling out of the liner (the "magnetic nozzle"). The magnetic field strength inside the liner is such that the ions that are generated are "weakly magnetized," as in some plasma processing devices (weak magnetization implies that ions under a specific temperature perpendicular to the magnetic field will not have orbits that intersect the liner walll).[13] When neutral xenon gas is injected into the liner, the induced oscillating magnetic fields generated by the currents in the antenna *both ionize the gas, and then heat the subsequent plasma.* Neither multiple RF stages, nor extra electron-generating mechanisms are necessary for RFT ignition. The heating directly impacts the electrons. Electrons are accelerated to very high energies, $\approx 50$ eV as evidenced by probe data, through inductive and stochastic interactions with

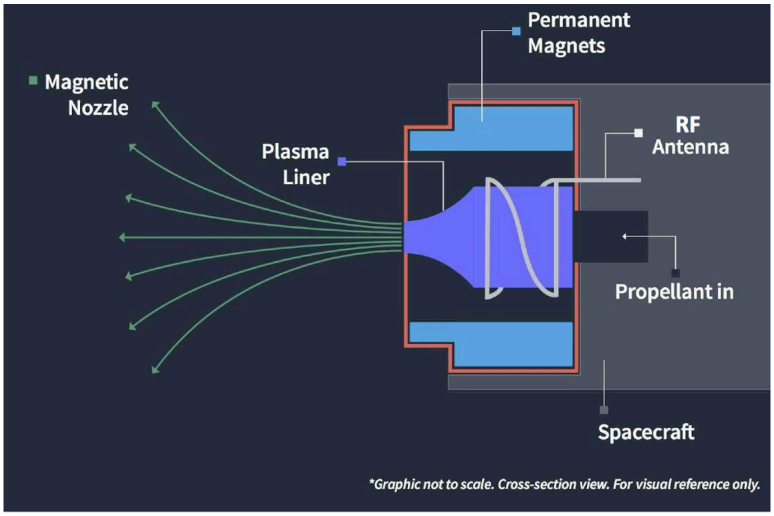


Figure 1: A representative diagram of the core components of the Phase Four RFT (not to scale).

the near fields from the antenna. The electrons, undergoing significant elastic collisions inside the liner, expand rapidly along the magnetic field lines parallel with the liner. The magnetic field geometry within the liner ensures that electrons maintain enough time in regions of high neutral density to produce significant ionization of the feed gas, and that electrons that are lost are largely lost via expansion in the magnetic nozzle, rather than upstream towards the spacecraft (to the right side of the liner in Fig. 1). The rapid flux of electrons into the plume of the thruster creates a momentary charge imbalance in the thruster. The slower xenon ions are then pushed out of the thruster via the charge imbalance at a rate sufficient to satisfy overal ambipolar fluxes of particles out of the system. The ion acceleration generated therein is the primary source of thrust in the RFT.

The ambipolar mechanism is also the source of ion accelertion in several other thruster concepts in development, such as the Cubesat Ambipolar Thruster at the University of Michigan, and the miniature ECR thruster in development at CNRS in France.[14,15] It is important to note that this ion acceleration need not occur over short Debye length scales,[16] (such as in double layer thrusters) and thus we do not consider the RFT to be an electrostatic thruster, rather we consider it to be an electrothermal system. The ion acceleration can occur over larger length scales (such as collision lengths and Larmor radii), and thus the physics of the ion acceleration must be treated delicately. It is interesting to note that such ion acceleration driven by electron heating has been observed in a wide array of systems, such as laboratory helicons with uniform (not expanding) magnetic fields,[17,18] in magnetic reconnection zones in the Earth's magnetosphere,[19] in laboratory RF plasmas expanding into vacuum,[20] and most recently in a lab RF plasma analog of space plasma physics.[21] To our knowledge, the Phase Four RFT is the smallest sized system to exhibit this increasingly ubiquitous effect.

The Phase Four RFT's design provides some advantages over some existing electric propulsion systems. First, as mentioned previously, RF switching electronics have steadily decreased in size and increased in power density due to advances with cellular and wireless power technologies. This allows the power processing unit for the RFT to be less than 500 grams for low Earth orbit CubeSat applications. Secondly, the unique small size of the system allows the volumetric RF power density in the plasma liner to be extremely high. For example, for a typical 100 W operation of the Phase Four RFT, the steady state volumetric RF power density inside the liner is on the order of $10^7$ W/m$^3$, as measured by the operational power into the RFT divided by the plasma liner volume. Contrast this to a typical volumetric power density of a laboratory helicon and helicon thruster, which range between $10^{5-6}$ W/m$^3$ at steady state, estimated in the same manner.[22] Consequently, the RFT does not need to rely on resonant energy transfer mechanisms between the RF signal and the plasma - stochastic heating of the electrons in the near field of the antenna suffices to generate large populations of fast particles. Also, the RFT's RF signals are in the HF band. Compared to similar electron cyclotron resonance (ECR) thrusters which operate in the S band and at higher frequencies, the RFT's RF signal has significantly less perturbation on common spacecraft communication signals.

This paper discusses the performance measurements of two generations of the Phase Four RFT. The RFT-

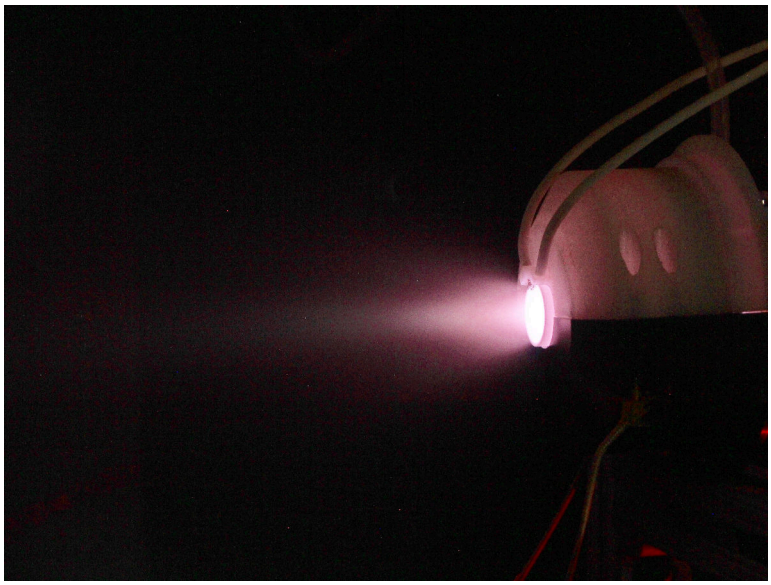

Figure 2: An image of the RFT-0 during a short burst firing test ($\leq$ 15 s) in the Phase Four small vacuum chamber with a xenon mass flow rate of 2.5 mg/s. and an RF power of 102 W.

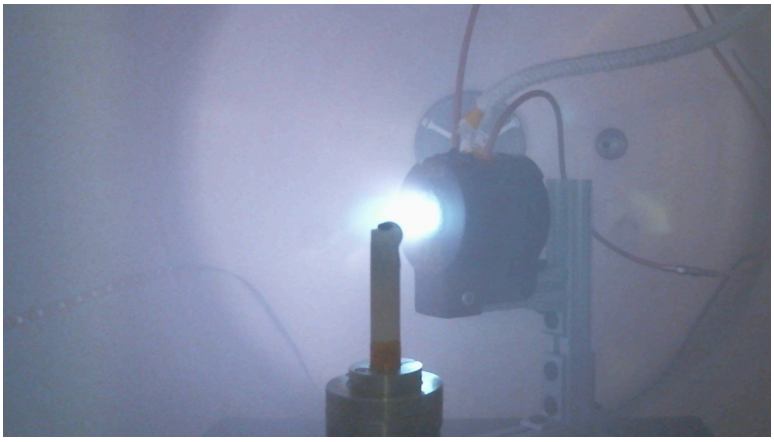

Figure 3: An image of the RFT-2 development unit firing at steady state (up to 90 minutes continuous operation in a given run has been performed thus far) in the Phase Four small vacuum chamber with a xenon mass flow rate of 0.3 mg/s. and an RF power of $\approx$ 100 W. A Faraday probe is visible in the foreground.

| **Name** | **RFT-0** | **RFT-1** | **RFT-2** |
|---|---|---|---|
| **Description** | Proof of concept | Tech demo flight unit | High performance |
| **Input Power [W]** | 102-123 | 80-110 | 40-120 |
| **Performance** | 3.94-5.27 mN, 101-175 s. measured | 4-5 mN,* 150-200 s* *design, to be measured | 1-5 mN,* 500+ s* *design, to be measured |

Table 1: Summary of RFT nomenclatures to be used throughout this paper. We will discuss RFT-0 and RFT-2 here.

0 was a proof of concept thruster and power processing unit that was tested on a direct thrust stand at The Aerospace Corporation in December, 2016. The RFT-2 is currently undergoing developmental testing at the

Phase Four laboratory. The RFT-2 is designed using lessons learned from RFT-0, to meet the performance needs of the upcoming small satellite constellations. The interim unit, RFT-1, is a flight-qualified version of RFT-0 currently undergoing checkouts, for use in Phase Four's technology demonstration mission. As we are concerned with the progress of performance testing for this paper, the RFT-1 will not be discussed further. Table 1 gives a summary of the naming convention of the three thruster iterations. Figures 2 and 3 show images of the RFT-0 and the RFT-2 units operating in the Phase Four small vacuum chamber.

## III. Direct thrust testing of RFT-0

The purpose of direct thrust testing the RFT-0 early on was twofold: to validate the concept of a miniaturized RF thruster in the HF band, and to establish an early set of fiducial data points from which progress could be directly compared. Phase Four deemed these to be important to prevent performance estimates to be derived from indirect methods with questionable sources of uncertainty. Furthermore, the construction of the test setup, including the prototype power processing unit and control computer architecture, gave Phase Four invaluable early experience at the design and integration of the primary subsystems that constitute a final product for a small satellite user. As a result, limited time was devoted to thruster optimization, and the measured performance was expected to be suboptimal. Nevertheless, the test results proved that the volumetric power density of the RFT-0 placed the unoptimized system in close contention with existing, larger helicon thrusters with significantly larger power budgets.[3,22]

### A. The RFT-0 test bus

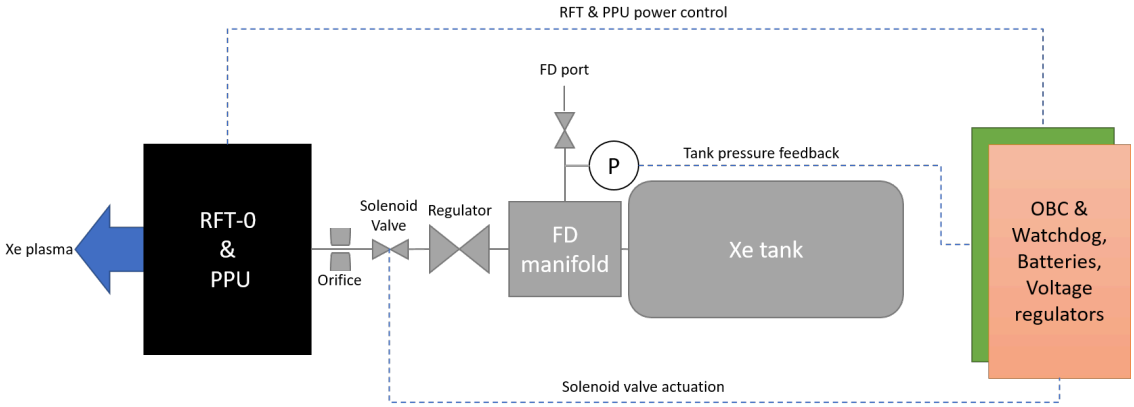


Figure 4: A high level diagram of the test bus used to test the RFT-0 on a thrust stand while minimizing vacuum feed throughs.

Measurement of the expected mN's of thrust from the RFT-0 system required developing a test unit that minimized power and gas feed throughs from the vacuum chamber wall to the thrust stand, as these would introduce significant uncertainty on the measurements. To acheive this, Phase Four developed a laboratory propellant management unit (PMU) and on board computer (OBC) using primarily commercial off the shelf (COTS) components. A xenon tank, made from a modified hand-held SCUBA tank was pressurized to 500 PSI via a custom machined fill-drain (FD) manifold. The pressure in the tank was monitored through a high pressure transducer installed in the FD manifold. The high pressure was regulated down to 30 PSI using a small form-factor COTS regulator. The 30 PSI xenon gas was flowed via a medical solenoid valve into a flex hose plenum, capped with a 10 $\mu$m orifice. The flex hose and orifice were mated to the gas feed interface in the plasma liner of the RFT-0. The RFT-0 power processing unit (PPU) both regulated the applied DC power, and inverted it into an RF signal applied to the antenna. The PPU power, the solenoid valve actuation duty cycle and frequency, and the tank pressure feedback were all monitored and controlled using an on board computer (OBC) that consisted of a Raspberry-Pi-based controller and a Texas Instruments MSP430 development board-based watchdog. The entire system was controlled wirelessly over the laboratory WiFi network. The implementation of these components allowed the RFT-0 to be tested with only a single power feed through from the vacuum chamber to the thrust stand, which consisted of a primary voltage rail

that was subsequently regulated and distributed to the systems on board the test bus via the OBC and on board regulation circuitry.

The solenoid valve was driven at 30 Hz and 35% duty cycle for all measurements. To calibrate the mass flow rate ($\dot{m}$) into the liner, the test bus was operated in the Phase Four small vacuum chamber (described in Section IV-A) at high vacuum. Pressure was actively measured on the high vacuum side of the chamber with a hot filament ion gauge. The small vacuum chamber had a dedicated xenon supply to the inside of the chamber via an Alicat mass flow controller with an accuracy of $\pm 0.01$ mg/s. The test bus was commanded to actuate the solenoid valve at the 30 Hz 35% duty cycle standard rate, and the pressure rise in the chamber was monitored until it reached a steady state. The solenoid valve was then commanded to 0% duty cycle, shutting off the mass flow rate of xenon from the test bust into the chamber. The Alicat mass flow controller was then commanded to operate at a fixed standard mass flow setting until the equilibrium pressure of the chamber settled at the same pressure as when the test bus was flowing xenon. The Alicat mass flow setting was then associated with the 30 Hz 35% duty cycle actuation rate of the solenoid valve.

Unfortunately throughout testing, inconsistencies in the measured cold gas thrust and the mass flow rate on the controller associated with a fixed solenoid valve actuation rate of up to $\approx 10\%$ were present. It was later determined that these were likely due to the heating of the gas plenum upstream of the orifice through heating of the solenoid valve, as well as insufficient valve driver circuitry. The associated mass flow rate with the fixed valve actuation rate was determined to be $3.5 \pm 0.5$ mg/s ($\dot{m} \pm \delta\dot{m}$). Consequently, for each thrust analysis presented in the following sections, the range 3.0 to 4.0 mg/s is used to determine a bound on the specific impulse ($I_{sp}$) and thrust efficiency ($\eta_T$). This represents the largest source of uncertainty in specific impulse and thrust efficiency calculations.

## B. Measurement setup

The vacuum chamber for thrust measurements at The Aerospace Corporation was approximately 3.7 m long and 2.4 m in diameter. It had a baseline pressure of approximately $10^{-7}$ Torr and was pumped by a 12,690 l/s Roots blower backed by eight parallel 141 l/s Stokes 412 roughing pumps, and 2X Edwards STP-iXA3306 Series turbopumps. The base pressure observed during testing the RFT-0 and test bus was $7.2 \times 10^{-6}$ Torr.

### *1. Description of torsional pendulum thrust stand and measurement technique*

The thrust stand used was based on a torsional design and consisted of a rigid aluminum arm, balanced atop a frictionless pivot with a calibrated spring constant. Similar designs have been documented in literature.[23–25] The thrust stand used for this work was a scaled up version of a 100 $\mu$N thrust stand with 1 $\mu$N sensitivity.[26] The thruster was mounted on one side of the arm, and counterweights were used to balance the arm on the opposite side. When the thruster fired, the arm was displaced, and the displacement was measured via an optical displacement meter; the thrust was calculated directly from the resulting displacement and the known spring constant. An image of the thrust stand with the RFT-0 test bus is shown in Fig. 5.

The main arm of the thrust stand is made of rectangular aluminum tubing to save weight while maximizing rigidity. The pivot spring constant was nominally 0.181 N-m/rad (0.0279 in-lb/deg, Riverhawk Industries) and was held in place by custom stainless steel mounts. The thrust stand was calibrated using known electrostatic forces between a pair of bare aluminum electrodes, shown on the left side of the thrust stand. The electrodes were held far from the thrust stand body to minimize fringing effects. A delrin flag attached to the back of the larger electrode which held a small (7 mm diameter) mirror was the target for the optical displacement meter (Philtec). The moment arms for the electrodes and the optical displacement meter were equivalent (0.5 m), and the moment arm to the thruster was 0.3 m.

The thrust in the torsional thrust stand was calculated directly from:

$$F_T = \frac{\theta \times k}{L} \tag{1}$$

where $F_T$ is thrust, $\theta$ was the deflection of the arm (radians), $k$ was the spring constant (N-m/rad), and $L$ was the moment arm (m). $\theta$ was directly measured via the optical displacement meter. The spring constant was estimated by the manufacturer, but the exact value was measured. To experimentally measure $k$, calibration electrodes were used to exert a known electrostatic force on the thrust stand. The calibration electrodes were made of bare aluminum and had diameters of 19 mm and 51 mm. The 19 mm electrode was mounted to a translational stage and the 51 mm electrode was mounted to the thrust stand. One electrode had a

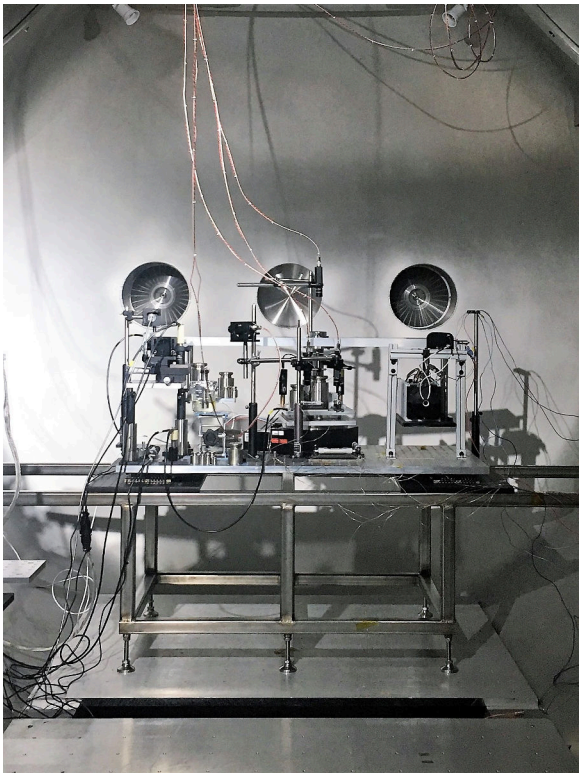

Figure 5: An image of the torsional balance thrust stand with the Phase Four RFT-0 test bus installed at The Aerospace Corporation.

larger diameter than the other to minimize fringing effects of electric fields around the edge of the electrode. For these studies, the larger electrode was attached to the thrust stand and was grounded, and the high voltage was applied to the smaller electrode. Thrust stand calibrations were carried out with the thruster payload installed and thrust stand level and balanced. Electrode spacing was set at 1 mm. The optical displacement meter (ODM) recorded the displacement of the thrust stand. A typical calibration is shown in Fig. 6. The slope of a plot of force vs. displacement ($\mu$m, as detected by the ODM) experimentally yielded the spring constant, which was directly converted to a value of $\mu$N/$\mu$m for small displacements. Given a known bias between the electrodes, the force can be calculated from the known force between electrodes for a parallel-plate capacitor:

$$F = 0.5\epsilon_0 \left(\frac{V}{D}\right)^2 A \tag{2}$$

where $F$ is force on each electrode (Newtons), $V$ is the voltage difference between them, $D$ is the electrode separation, and $A$ is the surface area, in this case, of the smaller electrode. Due to potential uncertainties from fringing, the electrostatic force was experimentally measured using a microbalance over electrode spacings 500 to 1200 $\mu$m, and up to 5 mN. Therefore, the electrostatic force produced by the exact electrode configuration with a known spacing and voltage bias was mapped, interpolated, and used for calibration.

Because the thrust stand behaved as a damped harmonic oscillator, classical equations of motion were used to characterize its motion relative to the displacement sensor. To analyze the stand response, the displacement of the thrust stand was given by:

$$x(t) = x_0 \exp(-\gamma t) \sin(\omega t + \phi) \tag{3}$$

where $x_0$ is the amplitude of step function displacement of the thrust stand, $\gamma$ is the damping rate of the thrust stand oscillations, $\omega$ is the resonant frequency of the thrust stand, and $\phi$ is the phase of thrust stand response to applied step force. It can be shown that this response is the solution to the forcing equation:

$$F(t) = Mx'' + bx' + kx \tag{4}$$

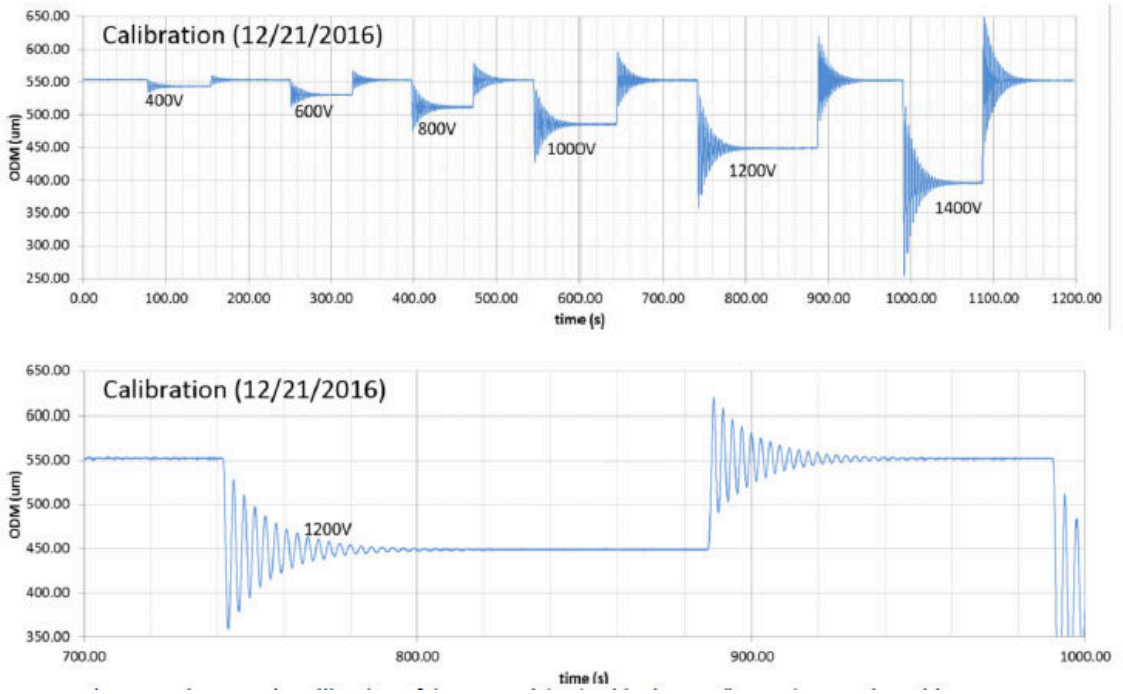


Figure 6: Output of ODM during calibration series of torsional pendulum thrust stand at The Aerospace Corporation. The top panel shows a full calibration set from 400 V to 1,400 V applied between the calibration electrodes. The bottom panel shows a zoomed in view around 890 s. to demonstrate the damped simple harmonic response of the thrust stand to step changes in applied torque.

and that $\omega^2 + \gamma^2 = k/M$, and $b = 2M\gamma$. $M$ is the effective mass of the test bus and thrust stand arm if all the mass was concentrated at the moment arm location. Using the measured response and Eqns. 3 and 4, the force due to the RFT-0 thrust events were estimated.

*2. Thrust measurement uncertainties*

Sources of thrust measuring uncertainty included determination of spring constant $k$ from uncertainties in setting electrode spacing, calibration voltages, ODM instrument resolution uncertainties which included environmental vibrational noise, linearity of $k$ over calibration range, interpolation of surface plots to extract electrostatic forces as a function of electrode spacing and voltage bias, and variation of $k$ during the test and throughout the day. Additional uncertainties arose from calculation of $\gamma$ and calculation of $\omega$, including nonlinear effects as a function of voltage bias and payload mass. Furthermore, in runs with plasma thrust, there was heating during the test, which caused the thrust stand baseline to drift. This was taken into account with the thrust calculation, after the thruster was turned completely off, so that the baseline immediately after the off command was given could be assumed to be the zero-thrust condition. However, in this case there was some residual gas flow in the plenum after the command to turn off was given, so that it was not clear how much of the baseline could be attributed to heating and how much to residual gas flow. As a result, the post-fire baseline was estimated by eye a few seconds after the largest drop to baseline and is a significant source of uncertainty in the thrust estimate.

## C. Results

*1. Raw data*

Figure 7 shows a representative response and analysis of the thrust stand during a cold gas and hot fire event. Calibration of the thrust stand using the electrodes was performed several times a day, approximately once every 1-2 hours, and at least at the beginning and end of each test day. The electrode spacing (1 mm) was set each day. The calibration spring constants varied between 36.5721 to 38.707 $\mu$N/$\mu$m. These units

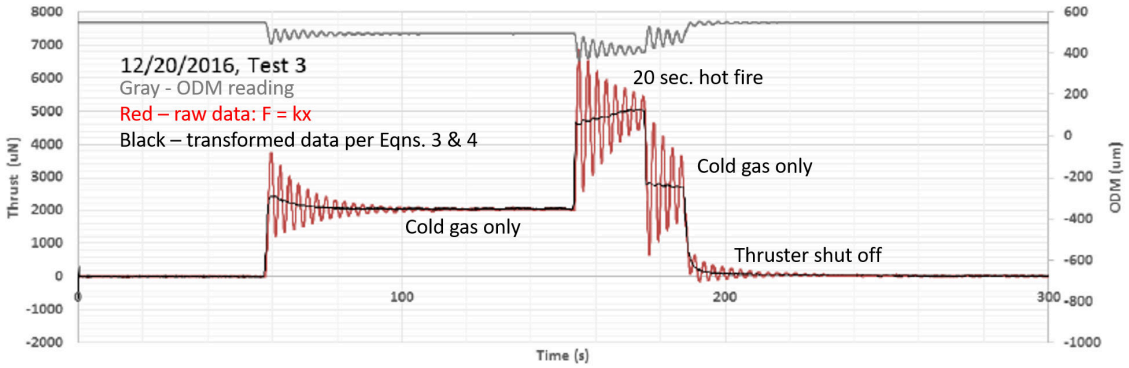


Figure 7: Representative thrust stand response during cold gas and hot fire test of the RFT-0 at The Aerospace Corporation.

directly convert displacement at the optical displacement sensor ($\mu$m) to force ($\mu$N) at the thruster moment arm. The transform was applied to each data set. Red lines are the raw data ($F = kx$, where $x$ is the displacement at the displacement sensor), and the black is the transformed data per Eqns. 3 and 4. The transform variables are combined values from the first and last calibrations taken that same day. As seen in Fig. 7, during a hot fire event, the measured thrust value increased in time. This may have been caused by a number for factors including heating of gas in the plenum, and an unstable design feature in the prototype power processing unit (which has since been ameliorated). As a result, for each test run, minimum and maximum measured thrust values are provided.

| Name | $P_{ch}$ [$10^{-4}$ Torr] | $F_{cg}$ [mN] | $P$ [W] | Min/Max $F_T$ [mN] | $\delta F_T$ [mN] | $\Delta t$ [s] |
|---|---|---|---|---|---|---|
| 122016-2 | 1.51 | 2.000 | 111 | 4.280/4.700 | 0.192 | 30 |
| 122016-3 | 1.58 | 2.050 | 123 | 4.580/5.030 | 0.205 | 20 |
| 122016-4 | 1.64 | 2.200 | 102 | 4.900/5.270 | 0.213 | 22 |
| 122016-5 | 1.54 | 2.100 | 102 | 4.700/5.000 | 0.203 | 30 |
| 122016-6 | 1.54 | 2.050 | 111 | 4.230/4.600 | 0.186 | 20 |
| 122016-7 | 1.48 | 1.950 | 123 | 3.940/4.350 | 0.177 | 23 |
| 122116-1 | 0.67 | 0.950 | 102 | 2.000/2.135 | 0.056 | 22 |
| 122116-2 | 0.81 | 1.100 | 102 | 2.400/2.600 | 0.063 | 30 |
| 122116-3 | 0.87 | 1.250 | 111 | 2.200/2.600 | 0.056 | 25 |
| 122116-11 | 1.41 | 1.720 | 102 | 3.700/4.580 | 0.096 | 80 |
| 122116-12 | 1.01 | 1.400 | 102 | 3.100/4.000 | 0.084 | 100 |

Table 2: Data from testing the RFT-0 in the test bus at The Aerospace Corporation, with calculated values of $F_T$ and uncertainties.

Table 2 provides the measured data from RFT-0 testing at The Aerospace Corporation. $P_{ch}$ is the pressure in the vacuum chamber as measured by a hot filamet ion gauge while running the thruster in pure cold gas mode. The data were calibrated to account for a xenon background gas. $F_{cg}$ shows the cold gas thrust as measured by the thrust stand prior to a hot fire event ($\approx$ 50 to 150 s in Fig. 7). $F_T$ shows the minimum and maximum hot fire thrust measured during a hot fire event, with the following column displaying the measurement uncertainty as a result of errors propagated down from calibration and analysis of the data, as described in the previous section. Finally $\Delta t$ shows the duration the hot fire thrust event was held for.

Thrust events were generally limited to short durations (30 s or less) to mitigate any thermal damage on the RFT-0 unit, both in the solenoid valve as well as the PPU proto-board. By the end of the first testing day (12-20-2016), Phase Four personnel pushed the RFT-0 and test bus to longer limits of run time at higher powers, for qualititative investigation of the thruster's response. Unfortunately, it is possible that

the solenoid valve was damaged through this process. On the second day of testing (12-21-2016) for the same valve actuation rate, approximately 50% of the $F_{cg}$ was observed. Thus for these data, $\dot{m}$ was not estimated per the calibration set of data from the Phase Four small vacuum chamber. The 12-21-2016 data are presented in Table 2 for reference. It is important to note that the total thrust measured scales approximately linearly with the cold gas thrust measured for each hot fire event, which suggests that the mass flow rate on the second day of testing (12-21-2016) was strongly degraded by the limit testing at the end of the previous day. Nevertheless, we do not know enough about what the mass flow rate into the thruster was on 12-21-2016 to include these data in the analysis below.

### *2. Analysis*

| Name | $P$ [W] | Min/Max $F_T$ [mN] | $\approx$ Min/Max $I_{sp}$ [s] | $\approx$ Min/Max $\eta_T$ |
|---|---|---|---|---|
| 122016-2 | 111 | 4.280/4.700 $\pm$ 0.192 | 110/156 | 0.020/0.034 |
| 122016-3 | 123 | 4.580/5.030 $\pm$ 0.205 | 117/167 | 0.021/0.035 |
| 122016-4 | 102 | 4.900/5.270 $\pm$ 0.213 | 126/175 | 0.028/0.046 |
| 122016-5 | 102 | 4.700/5.000 $\pm$ 0.203 | 121/166 | 0.026/0.042 |
| 122016-6 | 111 | 4.230/4.600 $\pm$ 0.186 | 109/153 | 0.019/0.032 |
| 122016-7 | 123 | 3.940/4.350 $\pm$ 0.177 | 101/144 | 0.015/0.026 |

Table 3: Analyzed data from 12-20-2016 using estimated $\dot{m}$ and carrying uncertainties through calculations of $I_{sp}$ and $\eta_T$.

Table 3 shows the estimated $I_{sp}$ and $\eta_T$ from the data on 12-20-2016, for which the solenoid valve behaved consistently in line with the calibration at Phase Four. The specific impulse is given by $I_{sp} = F_T/\dot{m}g_0$, where $g_0$ is the acceleration rate due to gravity on the Earth's surface. Likewise, thrust efficiency is given by $\eta_T = F_T^2/2\dot{m}P$. To calculate the minimum and maximum values shown in Table 3, the uncertainty in the measurement ($\delta F_T$), the uncertainty in the mass flow rate ($\delta\dot{m}$), and the variation of the measured thrust during a hot fire event were all compounded to provide a high level range on the $I_{sp}$ and $\eta_T$ for each run. Specifically, the minimum and maximum values for specific impulse were given by:

$$I_{sp}^{min,max} = \frac{F_T^{min,max} \mp \delta F_T}{(\dot{m} \pm \delta\dot{m})g_0} \tag{5}$$

and for thrust efficiency as:

$$\eta_T^{min,max} = \frac{(F_T^{min,max} \mp \delta F_T)^2}{2(\dot{m} \pm \delta\dot{m})P} \tag{6}$$

where $\delta\dot{m} = 0.5$ mg/s, is the uncertainty on the mass flow rate through the solenoid valve into the thruster for measurements on 12-20-2016.

Figure 8 summarizes the data from Table 3 in graphical form. Panel (a) displays $F_T$ data from Tests 1 through 6. The vertical lines describe how the thrust changed over the course of a hot fire. Error bars are included in this panel to show the uncertainty in the measurement due to known uncertainties in the thrust stand and the analysis fitting parameters. Panels (b) through (d) show $I_{sp}$, $F_T/P$, and $\eta_T$ respectively. Likewise in these panels, the vertical lines show the range of possible values due to *both* the range in $F_T$ observed during a hot fire, and the large uncertainty in $\dot{m}$.

### *3. Discussion*

Despite the RFT-0 and test bus's lack of optimization and sophistication, despite the large uncertainties and unknowns for these tests, and despite the variation in performance during the course of a hot fire, the data exhibit one salient piece of information: *the RFT-0 already meets or exceeds the performance of other RF thrusters, which have been tested on a direct thrust stand, that operate at much higher powers and are significantly more massive.* Specifically, inductive and helicon thrusters tested at the Australian National University[3], the University of Michigan[22], and Georgia Institute of Technology[36] heated plasmas with RF powers varying between 100 W and 2 kW, and yielded thrust values between 0.5 and 12 mN, specific impulses

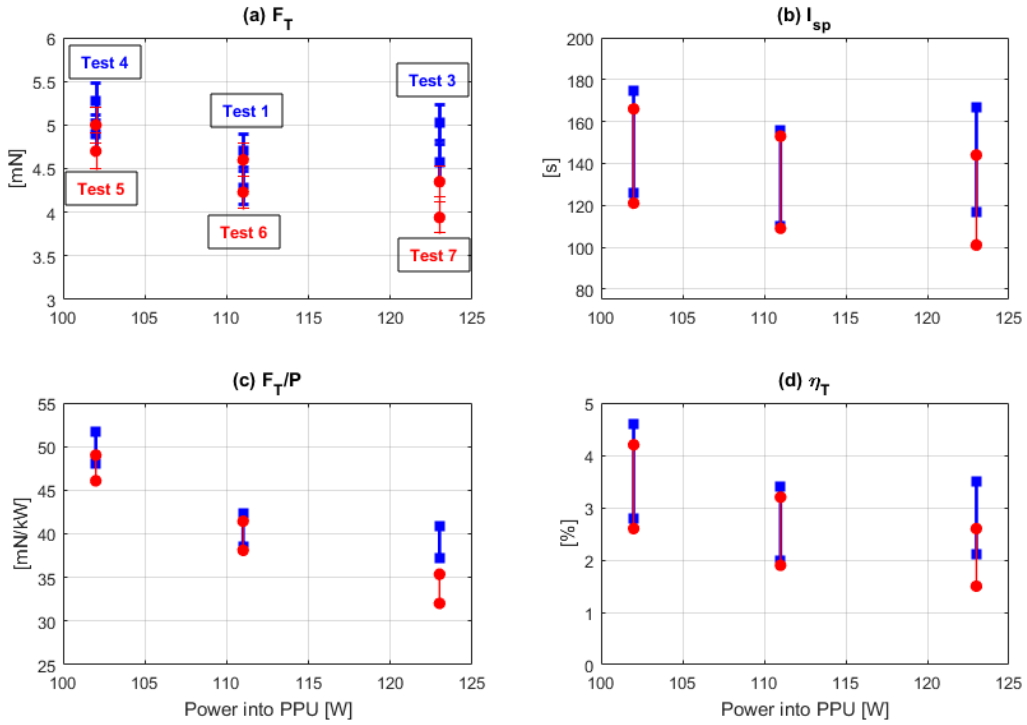


Figure 8: Plot summary of all data and estimates from Table 3. "Test #" refers to the test name of "122016-#" from the first column of Table 3. The vertical lines indicate the range in values calculated driven by the change in measured thrust over the course of a hot fire. Error bars on specific thrust measurements are shown in panel (a), as these were the only measurements that were not complicated by the large uncertainty in $\dot{m}$.

between 50 and 350 seconds and thrust efficiencies between 0% and 2%. The RFT-0 immediately produced similar thrust figures, $I_{sp}$ of 100 to 200 seconds, and $\eta_T$ between 1% and 5%. Notably, the RFT-0 yielded a thrust per power between 30 and 55 mN/kW, and had a total mass when installed in the test bus of under 3 kg. Phase Four maintains that these advantages are realized becasue of the extremely high volumetric RF power density in the plasma liner, obviating the need for resonant energy transfer to the plasma particles. Again, the details of these physics are reserved for subsequent disclosures. Admittedly, the electronics on board the test bus were lower mass than would exist on a longer duration low Earth orbit mission, but overall mass of the PPU is not significantly less than the current flight PPU under development at Phase Four.

An additional point to address is the relatively high neutral pressures in the chamber during these measurements. Due to the unoptimized nature of the RFT-0, the system required the significant mass flow rates reported here, suppressing $I_{sp}$ and $\eta_T$ and increasing the backpressure significantly in The Aerospace Corporation testing facility. Sufficiently high background pressures have been shown to generate anomalous thruster performance in the laboratory when compared to the in-space environment.[27] To get a basic understanding of whether the backpressure was a significant effect on the operation of the RFT-0, we estimated the ingested flow rate into the thruster per Goebel and Katz[28] as

$$\dot{m}_{ing} \approx 7.8 \times 10^7 \frac{P_{ch}\alpha\eta_c}{\sqrt{T_g M_{xe}^{amu}}}[mg/s] \tag{7}$$

where $\dot{m}_{ing}$ is the mass flow rate ingested into the thruster from the chamber backpressure, $\alpha$ is the thruster orifice area, $\eta_c$ is Clausing's factor, $T_g$ is the background gas temperature, and $M_{xe}^{amu}$ is the mass of xenon in atomic molecular units. Assuming a worst case scenario, we hold $\eta_c \to 1$, and $T_g = 100$ K. Using the measured $P_{ch}$ values we estimate a backflow of xenon from the chamber back into the thruster to be less than 0.05 mg/s, or $\leq 2\%$ of the mass flow rate injected into the thruster purposefully. While small partial pressures

are known to have effects on the physics of plasma systems,[29] we claim that this small of a perturbation does not contribute significantly to the overall performance observed during testing. We note here that the updated RFT-2 currently under development has successfully operated at steady state at mass flow rates as low as 0.01 mg/s in the Phase Four small vacuum chamber.

## IV. Probe measurements of RFT-0 and RFT-2

While RFT-0 direct thrust testing provided an excellent baseline, and while its performance exhibited an improvement for direct thrust tested RF thrusters, improved performance is necessary to meet the propulsion needs for a variety of applications. *The most pressing area of improvement is specific impulse.* Simply speaking, the RFT must exhibit similar thrust performance as has been measured, but at significantly lower propellant mass flow rates. In parallel with developing flight qualified subsystems to support an electric propulsion system on a small satellite, Phase Four is also improving the design of the RFT to achieve higher specific impulse. Currently under development, the RFT-2 consists of the same core components as the RFT-0, but has a significantly updated magnetic and liner design.

To update the community on the RFT-2 development progress, we are presenting a subset of electrostatic probe data taken in the plume of the developmental RFT-2. These data are compared to fiducial probe data taken in the plume of RFT-0. While RFT-2 has not yet been direct thrust tested, the changes observed in the probe data in the plume are indicative of the desired improved performance of the current RFT-2 unit under test.

### A. Experimental setup

The measurements presented here were performed in the Phase Four small vacuum chamber. The small vacuum chamber system consisted of a 0.75 m diameter by 1.25 m long chamber pumped by a Seiko Seiki maglev and an Alcatel ceramic bearing turbomolecular pump, which themselves were backed by an Alcatel and Edwards roughing pump respectively, with 28 l/s of total roughing capacity. The total pumping speed observed by the system was 2,400 l/s on $N_2$. The system typically achieved a pressure of $2 \times 10^{-7}$ Torr within one hour of pumping, and acheived $9 \times 10^{-8}$ Torr after three hours of pumping. Typical base pressures for the measurements presented here were between these two values. All high vacuum pressure measurements were made by a nude hot filament ion gauge inside the system. Foreline pressures on the turbomolecular pumps were also actively monitored with thermocouple gauges. The inside of the small vacuum chamber and the port to the Alcatel turbomolecular pump is visible in Figure 3.

Figure 9 shows a diagram of the probe diagnostics in the Phase Four small vacuum chamber. The RFT-2 development unit is fixed coaxially with the chamber near the door, and fires down the length of the chamber. Power and xenon gas are fed to the thruster through vacuum feed-throughs. Mass flow is controlled down to $\pm$ 0.01 mg/s by the same Alicat mass flow controlled used for calibrating the test bus mass flow rate. The details of the power feed-through are proprietary to Phase Four, but coarse resolution power into the system was measured and is reported here. The Faraday probe was designed following an elongated "nude" design.[30] The probe was comprised of a 1 cm diameter tungsten collection plate separated by a stainless steel 1.5 cm long guard ring. The collection plate was held in place with a boron nitride ceramic insulator between the collector's electrical connection and the guard ring. The ceramic insulator was recessed from the surface of the collector plate and the plasma-facing edge of the guard ring. The collector and guard ring were held at the height of the thruster on an alumina stalk, which itself was held in a stainless steel base. The alumina stalk and stainless steel base were hollow, with interior dimensions that allowed for a shielded electrical connection between the collector plate surface and an SMA output on the base. Also inside this region, were a series of self-resonant inductive chokes, set at specific frequencies. This allowed the probe stalk to be used for both Faraday probe and swept Langmuir probe measurements. The SMA output of the Faraday probe/Langmuir probe stalk allowed the signal to be sent to an SMA feed through in the vacuum chamber via a shielded coaxial cable. On the outside of the chamber the probe was biased and the current collected was measured by a Keithley 2400 source meter. Again, the same setup was also used for swept Langmuir probe measurements. The Keithley source meter was controlled and read using a LabView-based data acquisition (DAQ) system on a dedicated control rack for the small vacuum chamber. The probe holder and stalk were mounted on the end of a radial arm, which itself was mounted to a ThorLabs rotational mount. The center of the mount was aligned with the vertical axis in the chamber that intersects the center

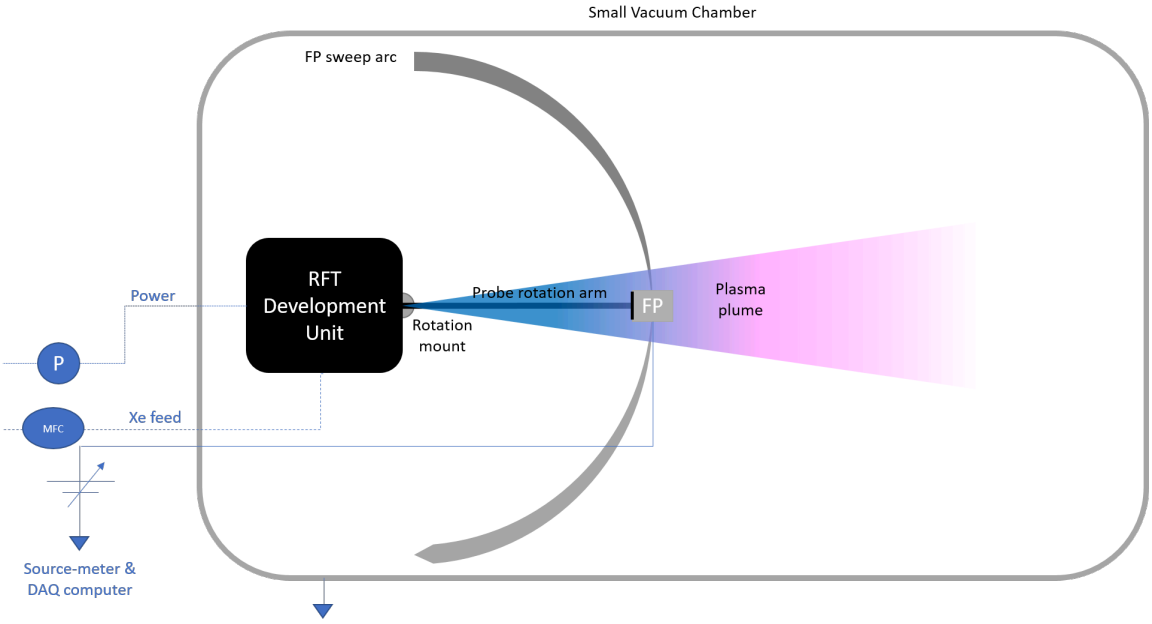


Figure 9: A representative diagram of the test setup at Phase Four for probe testing in the RFT plume. The Faraday probe (FP) is shown on a rotational mount, colocated with the RFT thruster orifice. Power and mass flow control are represented by the 'P' and 'MFC' blocks in the diagram.

of the thruster orifice, and was parallel to the thruster orifice exit plane. Adjusting the angular position of the rotational mount adjusted the position of the probe along a circular arc facing the thruster exit orifice. For the measurements presented here, the probe was always 16.5 cm radially away from the center of the thruster orifice. Care was taken to align the collecting surface of the Faraday probe to be normal to the vector intersecting the center of the thruster orifice and the center of the probe collector surface. The rotational mount angular position was controlled with precision of $\pm$ 0.25 deg. The angular acceleration and the angular velocity of the rotation stage were also controlled. For the measurements presented here, varying angular velocites between 0.5 and 4 deg/s were implemented. The position and the rotational parameters of the mount were also all controlled through the DAQ computer remotely. Finally, a USB powered camera was placed inside the chamber, monitoring the thruster, plume and the probe position at all times. The camera was not designed for in vacuum use, and as it heated up the CCD image became increasingly noisy. This required brief camera cool down periods between runs. All Faraday probe measurements were performed at -164 V bias on the Faraday probe. Swept Langmuir probe measurements extended between -63 V and + 63 V. All voltages were measured relative to the vacuum chamber wall, which was defined as the system ground. All electronics, including the entire DAQ rack were referenced to this potential.

## B. Results

### *1. RFT-0 plume investigations*

Figure 10 shows a representative Faraday probe trace in the plume of the RFT-0 developmental unit. The development unit was operated off of laboratory xenon, so the mass flow rate was well known for these measurements. From these data the divergence efficiency was calculated as:[31]

$$\eta_{div} = \left( \frac{\int_{-\pi/2}^{\pi/2} I_{sat}(\theta_p) cos(\theta_p) |sin(\theta_p)| d\theta_p}{\int_{-\pi/2}^{\pi/2} I_{sat}(\theta_p) |sin(\theta_p)| d\theta_p} \right)^2 \tag{8}$$

where $\eta_{div}$ is the divergence efficiency, $I_{sat}$ is the ion current collected when the Faraday probe is in ion saturation, and $\theta_p$ is the azimuthal angle of the Faraday probe relative to the thruster orifice normal vector. From the data in Fig. 10, $\eta_{div}$ for the RFT-0 unit was 43% $\pm$ 1%. The uncertainty was driven by the

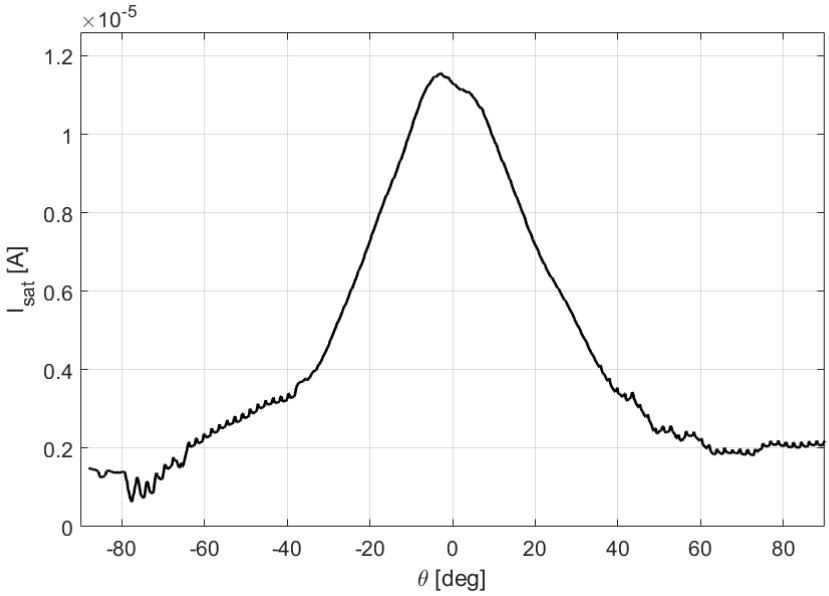


Figure 10: Representative raw data for the Faraday probe measuring ion current in the plume of the RFT-0 development unit with 2.95 mg/s mass flow rate at 103 W.

uncertainty in the angular position of the Faraday probe. The wings of the data set exhibit some asymmetries. We speculate that this may have been a facility effect. The chamber, being only 0.75 m in diameter, had walls close to the Faraday probe when the probe was at the extremes of $\theta_p$. On one side of the chamber the probe ventured close to power feed throughs coming into the chamber. Given the low plasma density in the chamber, the probe may have started to sweep through the sheath and presheath of the chamber walls at large $\theta_p$. More accurate Faraday probe data await Phase Four's larger vacuum chamber coming online (2.5 m diameter chamber currently undergoing installation). These perturbations would also have an effect on the measured divergence efficiency of the thruster.

It is important to note that at these mass flow rates, there were significant xenon charge exchange collisions prior to ion collection by the probe.[32] This significantly reduced the net ion beam flux collected by the probe. With a nude Faraday probe, charge exchange collisions may have also artificially broadened the measured beam, decreasing measured divergence efficiency. Furthermore, facility backpressure may have also had an effect on the presented measurements. The chamber pressure at such high flow rates given the reduced pumping speed was $6 \times 10^{-4}$ Torr. Performing the same worst care scenario analysis as before using Eqn. 7 results in an estimated $\dot{m}_{ing} \approx 0.2$ mg/s. While this is still small compared to the 3 mg/s intentionally flowed through the system, it may still have had a significant effect on the measured densities in the plume due to anomalously high source of neutral feed gas into the liner. Given these sources of facility error, the $\eta_{div}$ measured here is solely used an approximate fiducial point from which to reference future measurements.

Swept Langmuir probe data were also taken on axis ($\theta_p = 0^o$) to obtain fiducials for plasma density and electron temperature at the location of the Faraday probe. Figure 11 shows a representative Langmuir probe trace at this location. Density in the plume on axis was measured to be $8.75 \pm 0.2 \times 10^{14}$ m$^{-3}$ for the power and mass flow settings presented here. Electron temperature was measured to be $4.2 \pm 0.2$ eV. Panel (c) shows that a linear fit to the natural log of the electron current, to estimate the electron temperature of the plasma, was well suited for over 8 decades in collected current. This indicated that the electrons were undergoing significant collisions, thereby thermalizing before interacting with the Langmuir probe. This is highly unusual for plasmas in RF systems, and plasmas that should be flowing at high speed. Therefore, the high mass flow rate in the RFT-0 system, was retarding the acceleration of fast electrons, potentially retarding the ambipolar ion acceleration mechanism.

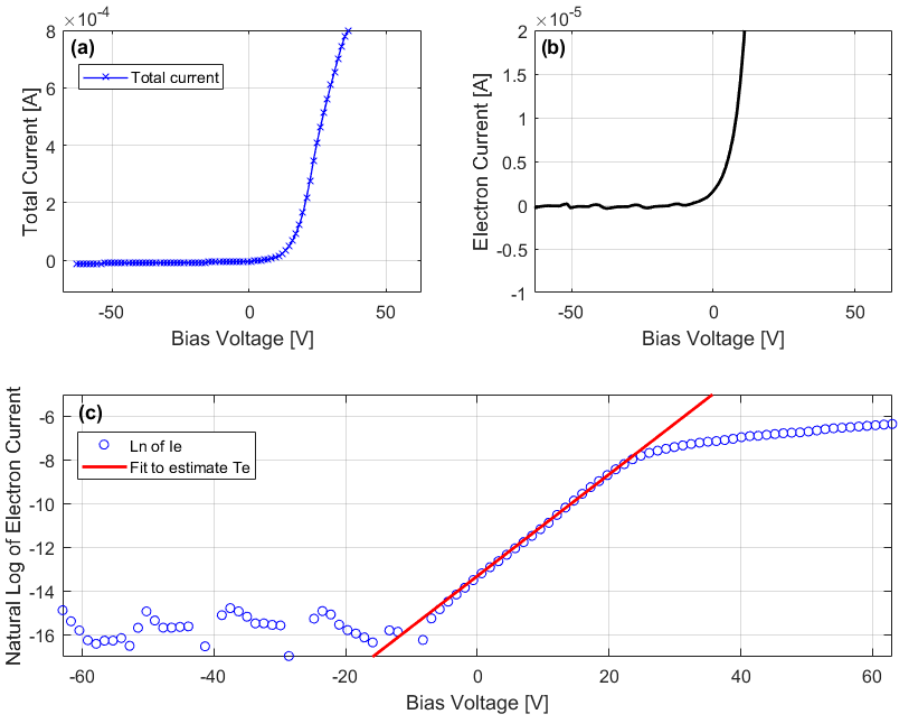


Figure 11: Representative Langmuir probe trace in the plume of RFT-0. (a) shows the overall trace, (b) is the trace minus the ion saturation current using a linear fit. The zoomed view ensures correct subtraction of the ion current contribution. (c) shows the natural log of the measured electron current and a linear fit to a Maxwell-Boltzmann distribution of background electrons.

### *2. RFT-2 plume investigations*

RFT-2 plume measurements exhibited significant beam and fast electron signatures in the Langmuir probe traces. Figure 12 shows a characteristic trace from RFT-2 demonstrating a fast electron beam. Panel (a) shows the overall Langmuir probe trace, and (b) shows a zoomed in view after the ion contributions are subtracted. The downward arrow points to a classic signature of a fast electron beam on top of a thermal background. Panel (c) shows the natural logarithm of the electron current trace. This allows the features at low current levels to be highlighted and analyzed. To distinguish between hot electrons and a fast monoenergetic electron beam, one looks for an electron population in the trace that is so hot that fitting to it yields temperature usually greater than 30-40 eV (V = -30 to -20 V in Fig. 12c), which quickly dies off to zero current at a sufficiently negative bias voltage. Assuming the feature marked by the downward arrow in (b) is in fact an electron beam, an estimate of the probe bias required to fully repel the beam is provided by the intersection of the dotted and dash-dotted lines ($\approx -32$ V). Similarly the transition of the collected probe current to electron saturation - the bias voltage at which all electrons in the distribution are collected - is marked by the intersection of the dotted and dashed lines ($\approx 31$ V). This feature is also highlighted in the first derivative of the probe trace, shown in panel (d), where the peak of the first derivative marks the transition to electron saturation. In quiescent plasmas (plasmas with no RF fluctuations, and a single species of thermalized electrons and ions), this transition approximates the local plasma potential. In the RFT plume plasma, where RF fluctuations, beams, secondary emission, and multiple populations may all be present, the transition to electron saturation is at best an approximation of the plasma potential within an uncertainty of $T_e/e$, where $T_e$ is the electron temperature in units of eV, and $e$ is the fundamental charge. An emissive probe is essential to ascertaining a more accurate estimation of the local plasma potential.[33] The bulk electron temperature was measured to be $\approx 5$ eV, which was calculated from the inverse slope of the fitting line to the natural log of the electron current, after the beam electrons were subtracted. We estimate the local plasma potential as sensed by the Langmuir probe to be $31 \pm 5$ V. We apply the same uncertainty

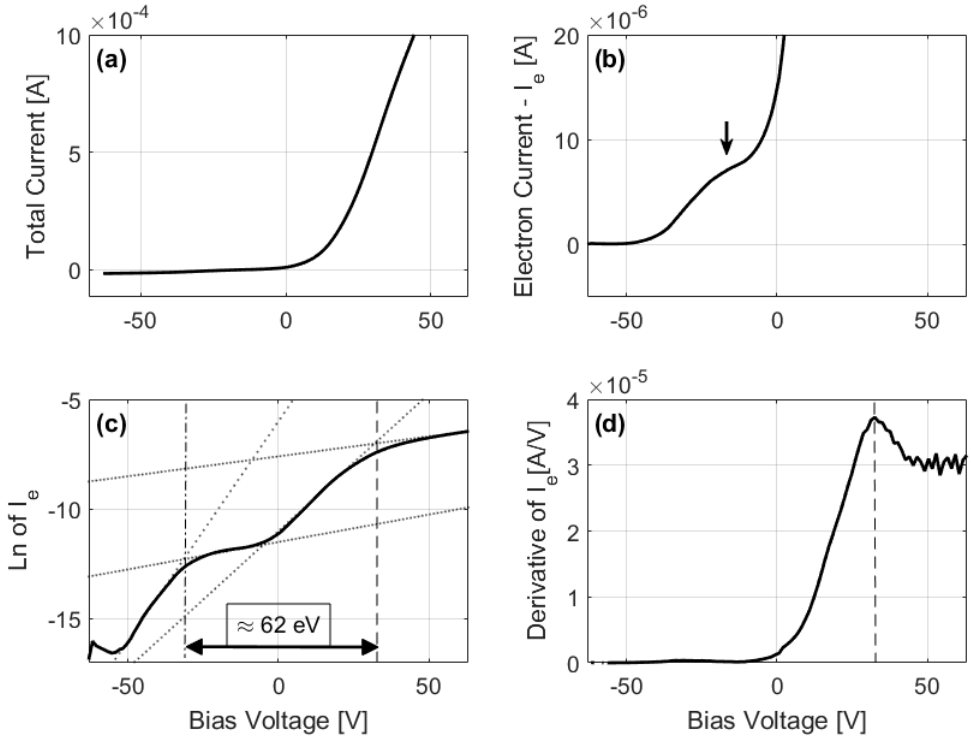


Figure 12: Representative Langmuir probe trace in the plume of RFT-2 at 0.3 mg/s and ≈ 120 W. (a) shows the overall trace and (b) is the trace minus the ion saturation current using a linear fit. The zoomed view highlights the appearance of an electron beam signature, as marked by the downward arrow. (c) shows the natural logarithm of the electron current, highlighting the features generated by the fast electron beam and by the electron saturation. The inverse of the slopes of the dotted lines *were not* used to calculate electron temperature, as the beam electrons must be subtracted first to perform this accurately. (d) shows the first derivative of the electron current, highlighting the transition to electron saturation.

to the measured bias voltage to repel the electron beam. Therefore, the electron beam kinetic energy relative to the estimated local electric potential (the kinetic energy of the drifting fast electrons, not the temperature of the fast population) is $\approx 62 \pm 10$ eV. Such electron beams are expected in expanding RF plasmas and have been observed with similar energies in low density RF plasmas,[37,38] and the analysis of such non-Maxwell-Boltzmann electron distributions must be handled with care.[34] Other features in the electron distribution may manifest themselves similarly in Langmuir probe traces, such as RF local electric potential fluctuations and secondary emission. RF fluctuations should be significantly damped in our probe traces through the RF chokes in the probe circuit. Also RF fluctuations impact the entire electron distribution, so the flucutuating beam-like signal should be seen at current levels comparable to the electron saturation level, which is not observed here. Secondary emission has the characteristic tell tale of a non-monotonically decreasing electron current collected as the bias voltages decreases, which is also not observed here. Therefore, treating the signature presented in Fig. 12 as a beam indicates that 16.5 cm away from RFT-2, at mass flow rates of 0.3 mg/s, very high energy electron beams are present, suggesting the inductive and stochastic heating in the thruster is sufficient both for high ionization rates of xenon gas by electron impact,[35] as well as fast electron ejection driving ion ambipolar acceleration.

After careful analysis, the plasma density in the plume of RFT-2 was also measured. The measurements are summarized in Fig. 13. The wide errorbars in applied power resulted from the very coarse method of power measurement for the initial tests of the RFT-2 development unit. Also shown in this Figure, is the density measured in the RFT-0 plume, at 3 mg/s. The salient aspect of this figure is that the RFT-2, operating at up to 10 times lower mass flow rates, was able to generate plume densitites comparable to that of RFT-0. This, along with the observed presence of fast beam electrons, indicated that the RFT-2

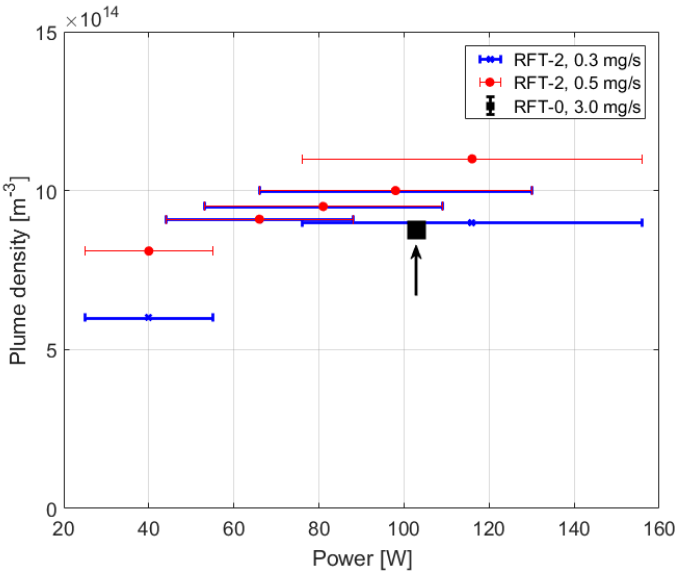


Figure 13: Plasma density in the same location in the plume for RFT-2 for 0.3 and 0.5 mg/s across varying applied power. The black square shows the fiducial data point for RFT-0 at 3 mg/s.

is ionizing significantly more propellant than the RFT-0 was, and was succesfully accelerating it out of the thruster at high speeds. This suggests that the RFT-2 development is making significant progress towards achieving higher propellant utilization efficiency and specific impulse.

As in the previous two discusisons, the background neutral population must again be considered. When operating at 0.3 mg/s, the measured pressure in the chamber after calibrating for xenon was $2 \times 10^{-6}$ Torr. Using the same worst case analysis on Eqn. 7, estimates the that $\dot{m}_{ing}/\dot{m} \leq 0.2\%$. Therefore we assume neutral backflow did not significantly affect the measurements and conclusions in this section.

## V. Summary & Outlook

The Phase Four RFT has been in development for almost 2 years at the Phase Four office and laboratory. It was determined early on that to make measured and rapid progress, a proof-of-concept would need to be tested on a direct thrust stand to avoid being bogged in incomplete indirect thrust analyses. To this end Phase Four developed the RFT-0, an unoptimized, but standalone thruster that could be tested on a 10 mN torsional balance thrust stand with minimal vacuum chamber feed throughs. This unit was tested at The Aerospace Corporation in December of 2016. Despite several non-idealities due to the young design (such as large uncertainty on known mass flow, and only short thrust durations possible), the thruster exhibited thrust, specific impulse, and thrust efficiency on par with significantly larger RF thrusters ($F_T$ = 3 - 5.5 mN, $I_{sp}$ = 100 - 200 s, $\eta_T$ = 1 - 5%). These results validated the overall concept of a very high volumetric power density RF thruster in the HF frequency band (the physics of which is not the focus of this paper).

Subsequently, in parallel with Phase Four's flight unit and subsystem development efforts (not discussed here), the RFT-2 unit has been undergoing testing. The RFT-2 is an updated RFT design, intended to achieve higher specific impulse than RFT-0, at comparable thrust levels. Also, the RFT-2 is intended to operate for much longer periods of time than the 20 to 100 seconds the RFT-0 was able to succesfully demonstrate. Comparative probe data in the plumes of RFT-0 and RFT-2 strongly suggest significant progress has been made in these regards. RFT-2 now routinely operates at mass flow rates 10 times lower than that of RFT-0, for hours at a time. Fast electron signatures are clearly visible in the plume, indicating efficient RF heating of the plasma. Furthermore the measured plasma density in the plume of RFT-2 is greater than or equal to the plume density in RFT-0, indicating significantly higher mass utilization efficiency. Plans are now underway to conduct an updated set of direct thrust tests on the RFT-2, to measure the exact progress Phase Four has made to meeting the needs of the upcoming small satellite contellations.

## Acknowledgments

The authors acknowledge the efforts of Derek Thompson, from West Virginia University, for assistance in the design, contruction and implementation of the plasma probes used here. Furthermore, Prof. Earl Scime (West Virginia University), Dr. Jim Gilland, (Ohio Aerospace Institute), Tim Collard (University of Michigan) and Prof. Alec Gallimore (University of Michigan) all provided useful tips and conversations. We would also like to thank Bruce Yost (NASA Ames Research Center) for the continued advice on meeting the needs of the small satellite market. Finally the entire team at The Aerospace Corporation, both in and out of the Propulsion Science and Testing Department, were very helpful in allowing us to move quickly with our measurements and progress.

## References

[1]Longmier, B. W., Cassady, L. D., Ballenger, M. G., Carter, M. D., Chang-Diaz, F. R., Glover, T. W., Ilin, A. V., McCaskill, G. E., Olsen, C. S., Squire, J. S., and Bering, E. A., "VX-200 Magnetoplasma Thruster Performance Results Exceeding Fifty-Percent Thruster Efficiency," *Journal of Propulsion and Power,* Vol. 27, No. 4, 2011, pp. 915-920.

[2]Choueiri, E. Y. and Spektor, R., "Coherent Ion Acceleration using two Electrostatic Waves," *36th AIAA/ASME/SAE/ASEE Joint Propulsion Conference & Exhibit,* AIAA 2000-3759, July 2000.

[3]Takahashi, K., Lafleur, T., Charles, C., Alexander, P., Boswell, R. W., Perren, M., Laine, R., Pottinger, S., Lappas, V., Harle, T., and Lamprou, D., "Direct thrust measurement of a permanent magnet helicon double layer thruster," *Applied Physics Letters,* Vol. 98, 2011, 141503.

[4]Dedrick, J., Gibson, A. R., Rafalskyi, D., and Aanesland, A., "Transient propagation dynamics of flowing plasmas accelerated by radio-frequency electric fields," *Physics of Plasmas,* Vol. 24, 2017, 050703.

[5]Nishiyama, K., Hosoda, S., Ueno, K., Tsukizaki, R., and Kuninaka, H., "Development and Testing of the Hayabusa2 Ion Engine System," *Joint Conference of 30th International Symposium of Space Technology and Science 34th International Electric Propulsion Conference and 6th Nano-satellite Symposium,* IEPC-2015-333, July 2015.

[6]Cannat, F., Lafleur, T., Jarrige, J., Chabert, P., Elias, P.-Q., and Packan, D., "Optimization of a coaxial electron cyclotron resonance plasma thruster with an analytical model," *Physics of Plasmas,* Vol. 22, 2015, 053503.

[7]Hopwood, J., "Review of inductively coupled plasmas for plasma processing," *Plasma Sources Science and Technology,* Vol. 1, 1992, pp. 109-116.

[8]Bonoli, P. T., "Review of recent experimental and modeling progress in the lower hybrid range of frequencies at ITER relevant parameters," *Physics of Plasmas,* Vol. 21, 2014, 061508.

[9]Gilland, J., Breun, R., and Hershkowitz, N., "Neutral pumping in a helicon discharge," *Plasma Sources Science and Technology,* Vol. 7, 1998, pp. 416-422.

[10]Magee, R. M., Galante, M. E., Gulbrandsen, N., McCarren, D. W., and Scime, E. E., "Direct measurements of the ionization profile in krypton helicon plasmas," *Physics of Plasmas,* Vol. 19, 2012, 123506.

[11]Siddiqui, M. U., McKee, J. S., McIlvain, J., Short, Z. D., Elliott, D. B., Lusk, G., and Scime, E. E., "Electron heating and density production in microwave-assisted helicon plasmas," *Plasma Sources Science and Technology,* Vol. 24, 2015, 034016.

[12]Liou, J. J. and Schwierz, F., "RF MOSFET: recent advances, current status and future trends," *Solid State Electronics*, Vol. 47, 2003, pp. 1881-1895.

[13]Kinder, R. L. and Kushner, M. J., "Noncollisional heating and electron energy distributions in magnetically enhanced inductively coupled and helicon plasmas," *Journal of Applied Physics*, Vol. 90, No. 8, 2001, pp. 3699-3711.

[14]Collard, T. A., Sheehan, J. P., and Jorns, B. A., "A Numerical Examination of the Performance of Small Magnetic Nozzle Thrusters," *53rd AIAA/SAE/ASEE Joint Propulsion Conference*, AIAA 2017-4721, July 2017.

[15]Lafleur, T., Cannat, F., Jarrige, J., Elias, P.-Q., and Packan, D., "Electron dynamics and ion acceleration in expanding-plasma thrusters," *Plasma Sources Science and Technology*, Vol. 24, 2015, 065013.

[16] Charles, C. and Boswell, R., "Current-free double-layer formation in a high-density helicon discharge," *Applied Physics Letters*, Vol. 82, No. 9, 2003, pp.1356-1358.

[17]Siddiqui, M. U. and Hershkowitz, N., "Double layer-like structures in the core of an argon helicon plasma source with uniform magnetic fields," *Physics of Plasmas*, Vol. 21, 2014, 020707.

[18]Siddiqui, M. U., Kim, J. F., Jackson, C. D., and Hershkowitz, N., "Presheath and boundary effects on helicon discharge equilibria," *Plasma Sources Science and Technology*, Vol. 24, 2015, 015022.

[19]Ergun, R. E., Goodrich, K. A., Wilder, F. D., Holmes, J. C., Stawarz, J. E., Eriksson, S., Sturner, A. P., Malaspina, D. M., Usanova, M. E., Torbert, R. B., Lindqvist, P.-A., Khotyaintsev, Y., Burch, J. L., Stangeway, R. J., Russell, C. T., Pollock, C. J., Giles, B. L., Hesse, M. Chen, L. J., Lapenta, G., Goldman, M. V., Newman, D. L., Schwartz, S. J., Eastwood, J. P., Phan, T. D., Mozer, F. S., Drake, J., Shay, M. A., Cassak, P. A., Nakamura, R., and Marklund, G., "Magnetospheric Multiscale Satellites Observations of Parallel Electric Fields Associated with Magnetic Reconnection," *Physical Review Letters*, Vol. 116, 2016, 235102.

[20]Takahashi, K., Akahoshi, H., Charles, C., Boswell, R. W., and Ando, A., "High temperature electrons exhausted from rf plasma sources along a magnetic nozzle," *Physics of Plasmas*, Vol. 24, 2017, 084503.

[21]Aguirre, E. M., Thompson, D. S., Scime, E. E., and Good, T. N., "Spontaneous Formation of Ion Holes and Ion Beams in Expanding Plasmas," submitted to *Physical Review Letters*, 2017.

[22]Shabshelowitz, A. and Gallimore, A. D., "Performance and Probe Measurements of a Radio-Frequency Plasma Thruster," *Journal of Propulsion and Power*, Vol. 29, No. 4, 2013, pp. 919-929.

[23]Soni, J., Zito, J., and Roy, S., "Design of a microNewton Thrust Stand for Low Pressure Characterization of DBD Actuators," *51st AIAA Aerospace Sciences Meeting including New Horizons Forum and Aerospace Exposition*, AIAA 2013-0755, 2013.

[24]Gamero-Castaño, M., Hruby, V., and Martínez-Sánchez, M., "A Torsional Balance that Resolves Sub-micro-Newton Forces," *27th International Electric Propulsion Conference*, IEPC-01-235, October 2001.

[25]Ziemer, J. K., "Performance Measurements Using a Sub-Micronewton Resolution Thrust Stand," *27th International Electric Propulsion Conference*, IEPC-01-238, October 2001.

[26]Hsu Schouten, A., Beiting, E., and Curtiss, T., "Performance of a Torsional Thrust Stand with 1 $\mu$N Sensitivity," *Joint Conference of 30th International Symposium on Space Technology and Science 34th International Electric Propulsion Conference and 6th Nano-satellite Symposium*, IEPC-2015-90062, July 2015.

[27]Kamhawi, H., Huang, W., Haag, T., and Spektor, R., "Investigation of the Effects of Facility Background Pressure on the Performance and Voltage-Current Characteristics of the High Voltage Hall Accelerator," *50th AIAA/ASME/SAE/ASEE Joint Propulsion Conference*, AIAA-2014-3707, 2014.

[28]Goebel, D. M. and Katz, I., *Fundamentals of Electric Propulsion: Ion and Hall Thrusters*, John Wiley & Sons, Hoboken, NJ, 2008, pp. 33-34.

[29]Yip, C.-S., Hershkowitz, N., and Severn, G., "Experimental Test of Instability-Enhanced Collisional Friction for Determining Ion Loss in Two Ion Species Plasmas," *Physical Review Letters,* Vol. 104, 2010, 225003.

[30] Hofer, R. R., Walker, M. L. R., and Gallimore, A. D., "A Comparison of Nude and Collimated Faraday Probes for Use with Hall Thrusters," *27th International Electric Propulsion Conference*, IEPC-01-020, October, 2001.

[31]Nakles, M. R., Barry, R. R., Larson, C. W., and Hargus Jr., W. A., "A Plume Comparison of Xenon and Krypton Propellant on a 600 W Hall Thruster," *31th International Electric Propulsion Conference*, September 2009.

[32]Miller, J. S., Pullins, S. H., Levandier, D. J., Chiu, Y.-h., and Dressler, R. A., "Xenon charge exchange cross sections for electrostatic thruster models," *Journal of Applied Physics*, Vol. 91, No. 3, 2002, pp. 984-991.

[33]Sheehan, J. P., Raitses, Y., Hershkowitz, N., Kaganovich, I., and Fisch, N. J., "A comparison of emissive probe techniques for electric potential measurements in a complex plasma," Vol. 18, 2011, 073501.

[34]Hershkowitz, N., "How Langmuir Probes Work," *Plasma Diagnostics*, Academic Press, New York, NY, Vol. 1, 1989, pp. 93-113.

[35]Stephan, K. and Märk, T. D., "Absolute partial electron impact ionization cross sections of Xe from threshold up to 180 eV," *The Journal of Chemical Physics*, Vol. 81, No. 1, 1984, pp. 3116-3117

[36]Williams, L. T. and Walker, M. L. R.., "Thrust Measurements of a Radio Frequency Plasma Source," *Journal of Propulsion and Power*, Vol. 29, No. 3, 2013, pp. 520-527.

[37]Ellingboe, A. R., Boswell, R. W., Booth, J. P., and Sadeghi, N., "Electron beam pulses produced by heliconwave excitation," *Physics of Plasmas*, Vol. 2, 1995, pp. 1807-1809.

[38]Chen, R. T. S. and Hershkowitz, N., "Multiple Electron Beams Generated by a Helicon Plasma Discharge," *Physical Review Letters*, Vol. 80, No. 21, 1998, pp. 4677-4680.